Physics in Medicine & Biology

PAPER • OPEN ACCESS

Interventional respiratory motion compensation by simultaneous fluoroscopic and nuclear imaging: a phantom study

To cite this article: Martijn M A Dietze *et al* 2021 *Phys. Med. Biol.* **66** 065001

IOP Publishing Phys. Med. Biol. 66 (2021) 065001 https://doi.org/10.1088/1361-6560/abe556

Physics in Medicine & Biology

IPEM Institute of Physics and Engineering in Medicine

OPEN ACCESS

RECEIVED
16 November 2020

REVISED
20 January 2021

ACCEPTED FOR PUBLICATION
11 February 2021

PUBLISHED
2 March 2021

PAPER

Interventional respiratory motion compensation by simultaneous fluoroscopic and nuclear imaging: a phantom study

Martijn M A Dietze[1,2], **Britt Kunnen**[1,2], **Marnix G E H Lam**[1] **and Hugo W A M de Jong**[1,2]

[1] Radiology and Nuclear Medicine, Utrecht University and University Medical Center Utrecht, PO Box 85500, 3508 GA, Utrecht, The Netherlands

[2] Image Sciences Institute, Utrecht University and University Medical Center Utrecht, PO Box 85500, 3508 GA, Utrecht, The Netherlands

E-mail: m.m.a.dietze@umcutrecht.nl

Keywords: SPECT/CT, respiratory motion compensation, interventional imaging, radioembolization

Abstract

Purpose. A compact and mobile hybrid c-arm scanner, capable of simultaneously acquiring nuclear and fluoroscopic projections and SPECT/CBCT, was developed to aid fluoroscopy-guided interventional procedures involving the administration of radionuclides (e.g. hepatic radioembolization). However, as in conventional SPECT/CT, the acquired nuclear images may be deteriorated by patient respiratory motion. We propose to perform compensation for respiratory motion by extracting the motion signal from fluoroscopic projections so that the nuclear counts can be gated into motion bins. The purpose of this study is to quantify the performance of this motion compensation technique with phantom experiments. *Methods*. Anthropomorphic phantom configurations that are representative of distributions obtained during the pre-treatment procedure of hepatic radioembolization were placed on a stage that translated with three different motion patterns. Fluoroscopic projections and nuclear counts were simultaneously acquired under planar and SPECT/CBCT imaging. The planar projections were visually assessed. The SPECT reconstructions were visually assessed and quantitatively assessed by calculating the activity recovery of the spherical inserts in the phantom. *Results*. The planar nuclear projections of the translating anthropomorphic phantom were blurry when no motion compensation was applied. With motion compensation, the nuclear projections became representative of the stationary phantom nuclear projection. Similar behavior was observed for the visual quality of SPECT reconstructions. The mean error of the activity recovery in the uncompensated SPECT reconstructions was 15.8% $\pm$ 0.9% for stable motion, 11.9% $\pm$ 0.9% for small variations, and 11.0% $\pm$ 0.9% for large variations. When applying motion compensation, the mean error decreased to 1.8% $\pm$ 1.6% for stable motion, 2.2% $\pm$ 1.5% for small variations, and 5.2% $\pm$ 2.5% for large variations. *Conclusion*. A compact and mobile hybrid c-arm scanner, capable of simultaneously acquiring nuclear and fluoroscopic projections, can perform compensation for respiratory motion. Such motion compensation results in sharper planar nuclear projections and increases the quantitative accuracy of the SPECT reconstructions.

Introduction

Fluoroscopy-guided interventions involving the administration of radionuclides (e.g. hepatic radioembolization (Braat *et al* 2015) or sentinel node procedures (Vidal-Sicart *et al* 2010)) would benefit from acquiring nuclear images while in the intervention room since this would allow for the evaluation of the activity distribution during the procedure. Recently, a compact and mobile hybrid c-arm scanner was developed that enables: (i) procedural guidance by simultaneous acquisition of planar nuclear and fluoroscopic projections with the same field of view (FOV), and (ii) procedural dosimetry by the acquisition of hybrid single-photon emission computed tomography/cone beam computed tomography (SPECT/CBCT) reconstructions (Dietze

et al 2019b, van der Velden *et al* 2019b). We refer to this novel scanner as interventional x-ray and scintigraphy imaging (IXSI).

The quality and the quantitative accuracy of the nuclear images that will be obtained during interventional procedures may be deteriorated due to patient respiratory motion (Murase *et al* 1987, Pretorius *et al* 2020). For planar imaging, a heavy respiratory motion will result in blurred nuclear projections, since the nuclear counts are smeared out over several pixels (Turner *et al* 1978). For SPECT/CBCT imaging, a heavy respiratory motion will additionally cause deteriorated dosimetric quality (Bastiaannet *et al* 2017). The procedure guidance capability of IXSI would hence improve when accurate compensation for respiratory motion is made.

The most common approach to compensate for respiratory motion is to gate the nuclear counts (obtained in list-mode) in motion bins based on a measure of the motion signal over time (Cho *et al* 1999, Zhang *et al* 2020). This motion signal can be retrieved from external devices (e.g. a respiratory belt) or from data-driven approaches (e.g. tracking the center-of-mass of the nuclear counts) (Nehmeh and Erdi 2008, McClelland *et al* 2013). However, external devices are undesired in an interventional setting since they are difficult to work with and do not provide sufficient flexibility. Data-driven approaches (Mukherjee *et al* 2013, Sanders *et al* 2016) can be unstable when imaging small doses of activity since these methods rely heavily on the counting statistics.

These conventional methods for obtaining the motion signal may hence not be best suited for employment in interventional procedures. In this work, we will investigate whether it is possible to extract the respiratory motion signal from the fluoroscopic projections that are acquired with IXSI for procedural guidance. This methodology has the potential advantage that a continuously stable estimate of the motion signal is obtained and no setup of external devices is required, facilitating its use in an interventional setting.

By employing the motion compensation approach with IXSI, the projections obtained with planar imaging are expected to become sharper and the quantitative accuracy of the SPECT reconstruction should improve. Before IXSI will be employed in patients, this study aimed to quantify the performance of the proposed motion compensation approach with phantom experiments.

Methods

IXSI

IXSI consists of a detector stack that is positioned on a mobile custom-made c-arm (Indes, Enschede, The Netherlands) with an x-ray tube (Veradius; Philips Healthcare, Best, The Netherlands) positioned on the opposite side (see figure 1). The detector stack consists of a flat panel detector for 2D and 3D interventional radiology (Pixium 3040; Trixell, Moirans, France) positioned in front of a gamma camera (P3000; Inter Medical, Lübbecke, Germany) mounted with a cone beam collimator (Nuclear Fields, Vortum-Mullem, The Netherland). The x-ray tube is positioned at the same distance as the focal distance of the cone beam collimator (105 cm) so that intrinsically overlapping nuclear and fluoroscopic projections are acquired.

The c-arm can translate in two directions while rotating and is able to perform parameterized non-circular orbits. A collision detector is present in front of the flat panel detector so that the c-arm rotation terminates when contact with an object is registered. The settings of the x-ray tube are set on the console that is integrated into the scanner.

The flat panel detector was adjusted from the commercially available product by reduction of the back-shielding thickness and by removal of several internal highly-attenuating components (e.g. support screws) so that the transmission of gamma photons increased. The thickness of the flat panel detector is 6.8 cm and the average transmission of gamma photons at 140 keV is 52%. The FOV of the flat panel detector is 39.9 $\times$ 29.5 cm^2.

The gamma camera was adjusted from the commercially available product by having alterations in the detector housing to fit on the custom c-arm. The effective FOV of the gamma camera is 51.0 $\times$ 38.1 cm^2. The cone beam collimator has holes with 40.0 mm length, 1.90 mm inner diameter, and 0.25 mm septal thickness. The gamma camera has an intrinsic spatial resolution of 3.9 mm full width at half maximum (FWHM) and an energy resolution of 9.4% at 140 keV. The gamma camera has a 12.1 mm FHWM extrinsic spatial resolution at 10 cm distance to the flat panel detector.

Phantoms

One of the proposed uses of IXSI is the guidance of the pre-treatment procedure of hepatic radioembolization, in which ^{99m}Tc-labeled macro aggregated albumin (^{99m}Tc-MAA) is injected into the hepatic artery. Two activity distributions (see figure 2) that are expected to arise during the procedure guidance of radioembolization were evaluated:

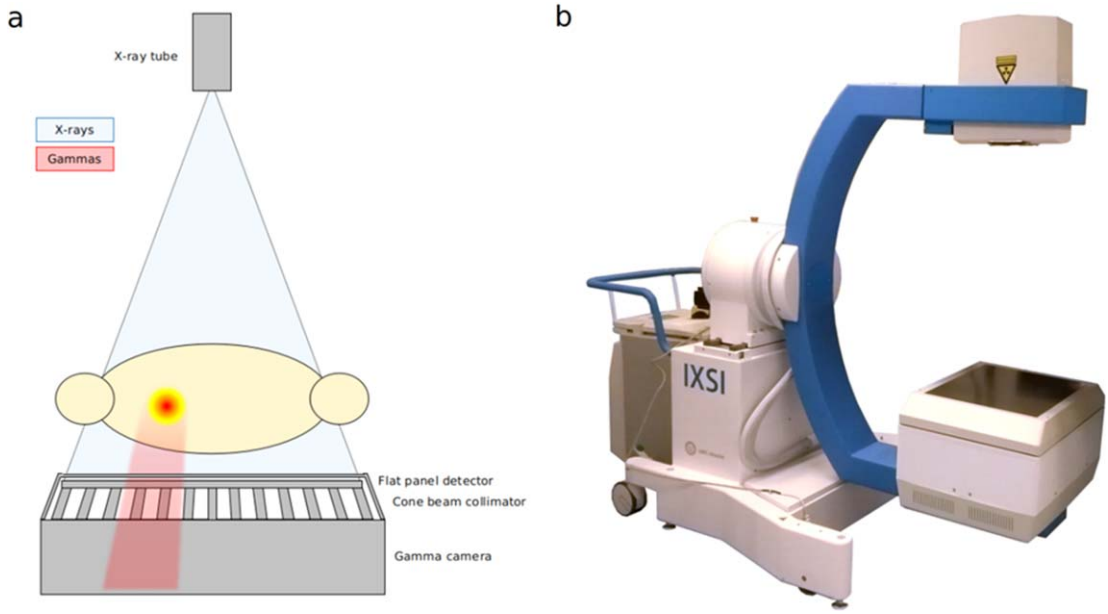

Figure 1. (a) A schematic illustration of the scanner components and (b) the developed scanner. IXSI consists of a detector stack (consisting of a collision detector, a flat panel detector, a cone beam collimator, and a gamma camera) that is mounted together with the x-ray tube on a mobile custom c-arm.

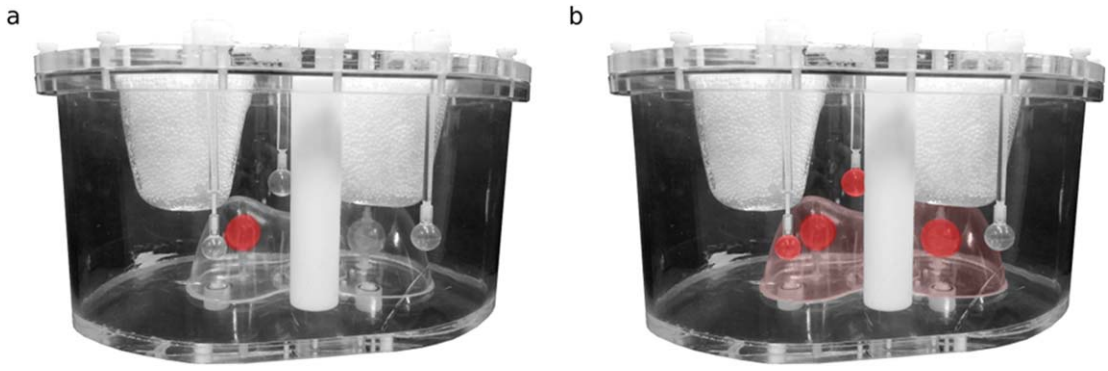

Figure 2. A representation of the two activity distributions that were evaluated: (a) a superselective and (b) a whole liver treatment. The red overlay represents the volumes that had activity present.

Superselective treatment

The first activity distribution represents an interventional procedure in which only one tumor is targeted (i.e. a superselective treatment) and all activity accumulates in this tumor. This setting was recreated by inserting a sphere (15.6 mm radius, 16 ml volume) of 38 MBq in the liver compartment of an otherwise non-active anthropomorphic thorax phantom (model ECT/TOR/P).

Whole liver treatment

The second activity distribution represents a whole liver treatment in which the activity has spread out. This setting was recreated by filling the liver compartment (1172 ml) with 229.7 MBq, inserting a sphere (15.6 mm radius, 16 ml volume) of 24.9 MBq and a sphere with a cold core (approximately 11.3 mm inner and 18.1 mm outer radius, 19 ml active and 6 ml cold core volume) of 30.2 MBq in the liver compartment (tumor to non-tumor ratio of 8:1), and inserting two spheres (12.5 and 9.9 mm radius, 8.1 and 4.1 ml volume) of respectively 4.8 and 2.5 MBq in the background compartment (simulating extrahepatic accumulations).

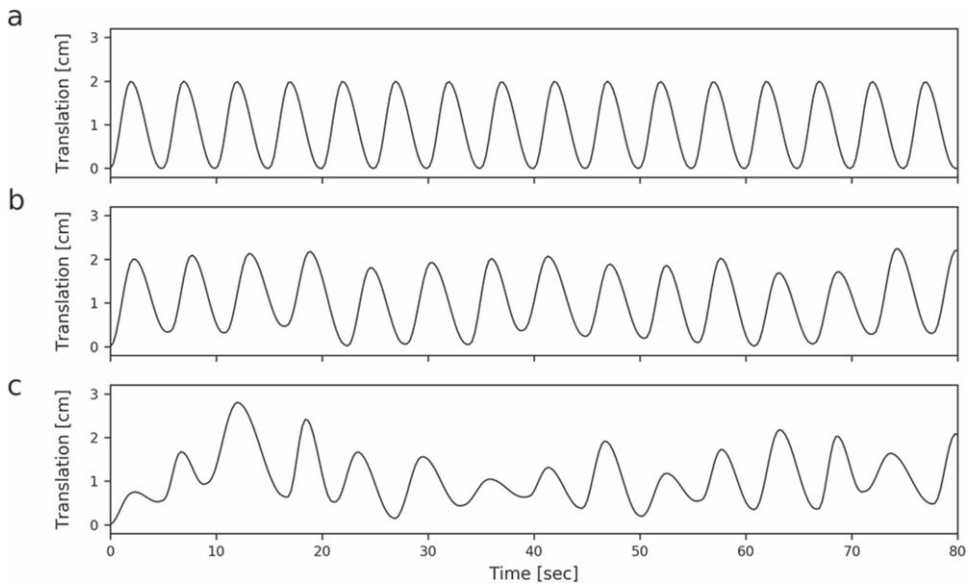

Figure 3. The motion amplitude over time of the three studied motion patterns: (a) stable motion, (b) small variations, and (c) large variations.

Acquisition

For all experiments, fluoroscopic projections were sampled at 3.75 Hz (the lowest rate that could be set with the used x-ray tube) with pulsed x-rays (of 27.8 ms in duration) and nuclear counts were simultaneously acquired in list-mode. The gamma camera counts that were obtained while the x-ray tube was on, were removed from the nuclear data since these counts could have originated from x-ray photons instead of gamma photons (Koppert *et al* 2018, 2019). The x-ray photons blinded the gamma camera for 3.75 Hz $\times$ 27.8 ms $=$ 10.4% of the time. The fluoroscopic projections were acquired at a 1008 $\times$ 1008 grid with a 0.399 mm pixel size. The nuclear projections were acquired at a 128 $\times$ 128 grid with a 4.79 mm pixel size.

Both anthropomorphic phantom configurations were placed on a motor-driven stage that translated in one direction with a sinusoidal-like signal. The properties of this signal (amplitude, baseline shift, and period) were set differently for three studied patterns: stable motion, motion with small variations, and motion with large variations (see figure 3 for an illustration). For stable motion, the maximum motion amplitude was 2 cm, the baseline shift was 0 cm, and the period was 5 s. For small and large variations, every oscillation of the signal had a random assignment of the maximum motion amplitude, baseline shift, and period. For small variations, the maximum motion amplitude was between 1.5 and 2.0 cm, the baseline shift was between 0 and 0.5 cm, and the period was between 5 and 6 s. For large variations, the maximum motion amplitude was between 0.5 and 2.0 cm, the baseline shift was between 0 and 1 cm, and the period was between 4 and 8 s.

The motion compensation performance for planar imaging was studied with the superselective treatment phantom since this phantom configuration provides a sharp contrast in the planar images. The motion compensation performance for SPECT/CBCT imaging was studied with the whole liver treatment phantom configuration since this phantom configuration has several features that are interesting to study quantitively.

Motion signal extraction

First, two methods were compared on their motion signal extraction performance: (i) a data-driven approach, and (ii) the proposed fluoroscopy-guided approach. For the data-driven approach, the motion signal was extracted by calculating the center of mass of the nuclear counts over time. For the fluoroscopy-guided approach, fluoroscopic projections were acquired and the motion signal was extracted by calculating the center of mass of the diaphragm. The motion signal extraction performance was studied for planar imaging with the superselective treatment phantom configuration that was translating with stable motion. Pearson's correlation coefficient between the extracted motion signal and the true phantom position was calculated for both motion signal extraction methods. Every motion signal extraction measurement was repeated five times to study the stability of the results. The acquisition time was 40 s (eight motion signal oscillations) for every measurement. The data-driven motion signal extraction measurements were made immediately after each other to ensure that radioactive decay had little influence on the obtained results.

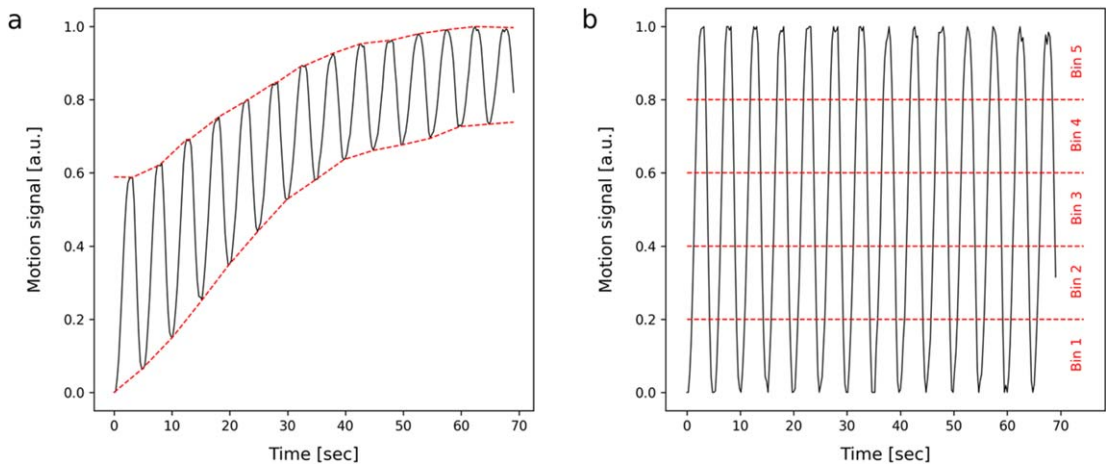

Figure 4. A schematic illustration of the gating procedure. (a) From the extracted motion signal from the fluoroscopy projections (solid line), the signal peaks are determined (dashed lines) and the signal is normalized. (b) The normalized signal is divided into five motion bins that span an equal amplitude range.

To get insight into the influence of dose and activity on the signal extraction performance, the x-ray tube strength was varied from 45 to 80 kVp and the activity level in the phantom was varied from 5 to 35 MBq by sampling counts from the list-mode data. Sampling was performed by making uniform random subsets: all counts from the list-mode data were considered individual events and their properties (x, y, time) were put into a list. This list was shuffled randomly and a fraction of the shuffled list (determined by the target activity level) was retained for further processing.

The dose corresponding to the above x-ray tube settings was determined with the dose area product (DAP) meter that is integrated into IXSI. It will prove that the fluoroscopy-guided approach provides a more stable signal over the respiratory cycle than the data-driven approach. The remainder of the manuscript hence employed the fluoroscopy-guided approach for motion compensation.

Planar imaging

To assess the planar imaging performance, nuclear and fluoroscopic projections were simultaneously acquired for the anthropomorphic phantom with the superselective treatment configuration while it was translating with stable motion and while it was stationary. The acquisition time was one minute for all scans. The acquisitions were made immediately after each other to ensure that radioactive decay had little influence on the obtained results.

For all acquisitions, the x-ray counts detected by the gamma camera were removed from the list-mode file. For the translating phantom without motion compensation and for the stationary phantom, the nuclear projections were created by summing the nuclear counts together. For the translating anthropomorphic phantom with motion compensation, the following steps were taken (see figure 4 for an illustration): (i) the motion signal was determined from the fluoroscopic projections, (ii) the motion signal was normalized to the peaks, (iii) the nuclear counts were gated into five motion bins that span an equal motion signal amplitude range, and (iv) the nuclear projection was created by including only the nuclear counts from one of the five motion bins (the bin that had the most nuclear counts present was selected). A 5 mm FWHM Gaussian filter was applied to the nuclear projections and the visual quality of the projections was compared.

SPECT/CBCT imaging

To assess the SPECT/CBCT imaging performance, nuclear and fluoroscopic projections were simultaneously acquired for the anthropomorphic phantom with the whole liver treatment configuration while it was translating with one of the three motion patterns and while it was stationary. The c-arm rotated over 360° (with 120 angles) during an acquisition of 10 min.

For all acquisitions, the x-ray counts detected by the gamma camera were removed from the list-mode file. For the translating phantoms without motion compensation and for the stationary phantom, the nuclear counts and fluoroscopic projections were processed together. For the translating phantoms with motion compensation,

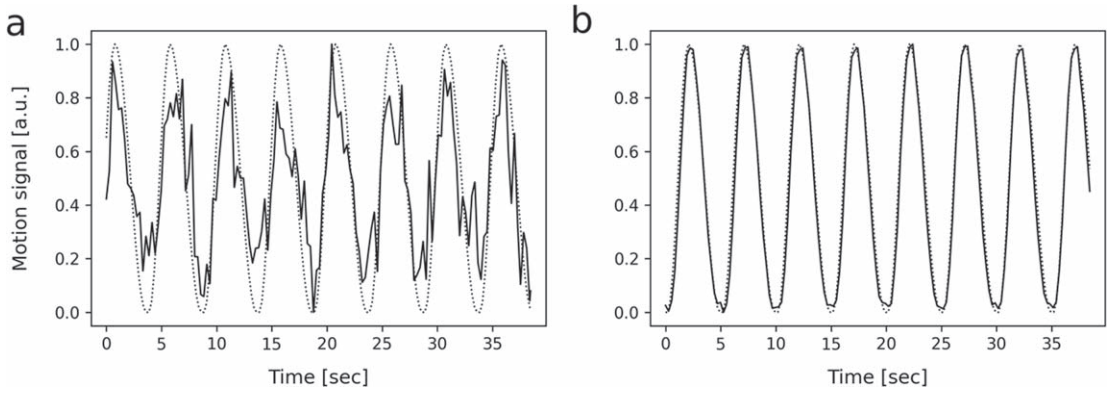

Figure 5. Examples of the extracted motion signals (solid line) together with the true motion pattern (dashed line) in arbitrary units (a.u.) for (a) the data-driven approach (with 15 MBq) and (b) the fluoroscopy-guided approach (with 60 kVp).

gating of the nuclear counts was performed in the same way as in the planar imaging experiment (see figure 4) although this time the fluoroscopic projections varied in acquisition angle during rotation of the scanner.

The fluoroscopic projections were reconstructed using reconstruction software from Philips Healthcare. Since the CBCT reconstruction had a limited FOV and because the quality of the CBCT reconstruction was deteriorated by scattered photons, the CBCT reconstruction was registered to a previously acquired attenuation map using the elastix software package (Klein *et al* 2010).

The nuclear projections were reconstructed with the Utrecht Monte Carlo System (UMCS) software package, which included Monte Carlo-based scatter correction, point spread function modeling, and attenuation correction (Dietze *et al* 2018, 2020b). The software package used the OSEM reconstruction algorithm with 10 iterations and 8 subsets and reconstructed to a $128 \times 128 \times 128$ grid with a 4.79 mm isotropic voxel size. The Monte Carlo-based scatter correction included the modeling of photons interactions in the flat panel detector. No smoothing was applied to the reconstruction.

The total activity in the anthropomorphic phantom with the whole liver treatment configuration was 292 MBq. By sampling from the list-mode nuclear counts (by creating uniform random subsets in the same way as was done in the data-driven motion signal extraction experiment), nuclear projections corresponding to 150 MBq total phantom activity were created (so that the same activity level as injected during a clinical pre-treatment procedure of radioembolization was achieved). Sampling was performed after the removal of x-ray counts from the data and before the motion binning. The sampling process was repeated 10 times to study the influence of different noise patterns on the reconstruction stability.

The visual quality and the quantitative accuracy of the SPECT reconstructions were assessed. For the quantitative analysis, the activity recoveries of the four spherical inserts were calculated. This metric is important in e.g. dosimetry as required for radioembolization planning. The masks of the spherical inserts were manually delineated on the registered attenuation map.

Results

Motion signal extraction

Examples of the extracted motion signals for the data-driven (using 15 MBq) and fluoroscopy-guided approach (using 60 kVp) are given in figure 5. The data-driven method had substantial variations in the motion signal amplitude over time. In contrast, the fluoroscopy-guided motion signal provided a very stable motion signal.

The correlation between the extracted motion signal and the true phantom position is shown in figure 6 for the data-driven approach as a function of the phantom activity and for the fluoroscopic projection approach as a function of the x-ray tube strength. The correlation from the fluoroscopic motion signal extraction was consistently higher than that of the data-driven approach. The correlation of the fluoroscopic projection approach reached a plateau after an x-ray tube strength of 50 kVp. The fluoroscopic projection approach was used in the remainder of the manuscript since it provided more stable results than the data-driven method.

The dose levels corresponding to the above-evaluated x-ray tube settings are collected in table 1. The beam current values increased while the beam voltage increased because the system provided insufficient freedom for modifying this setting. The dose is provided in DAP per minute and DAP for a total of 15 min of scanning (e.g. 5 min of planar imaging and 10 min of SPECT/CBCT). The DAP-meter that is integrated into IXSI was not able

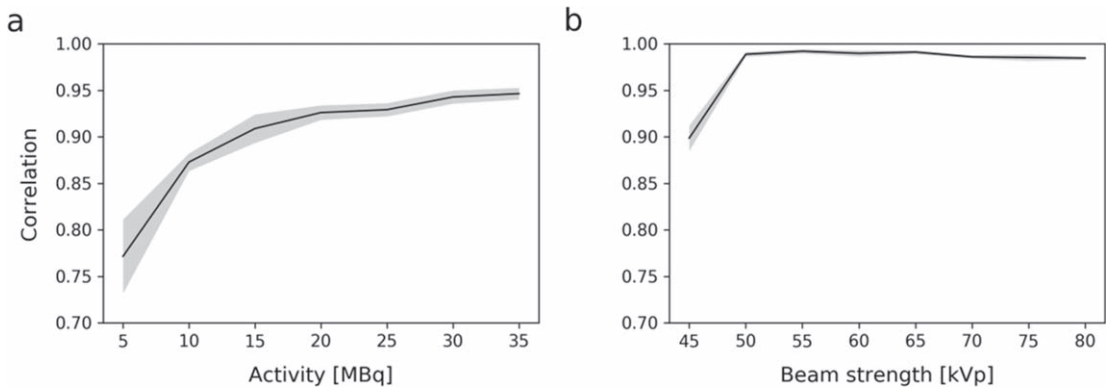

Figure 6. The correlation between the extracted motion signal and the true phantom position for (a) the data-driven approach as a function of the phantom activity and (b) the fluoroscopic projection approach as a function of the x-ray tube strength.

Table 1. The dose area product for the evaluated x-ray tube settings in DAP per minute and total DAP for 15 min of scanning.

Beam voltage (kVp)	Beam current (mA)	DAP (μGy m^2 min^{-1})	15 min DAP (mGy m$^{2)}$)
60	0.52	51.9	0.8
65	0.81	98.3	1.5
70	1.14	188.3	2.8
75	1.15	236.5	3.5
80	1.17	284.6	4.3

to measure the dose below 60 kVp. Hence, although 50 kVp was previously found to be sufficient for the accurate extraction of the motion signal, 60 kVp was used for the fluoroscopic projections in the remainder of this work.

Planar imaging

The nuclear projections obtained through planar imaging of the anthropomorphic phantom with the superselective treatment configuration when made with and without motion compensation are shown together with the projection from the stationary anthropomorphic phantom in figure 7 for the three studied motion patterns. The sphere was smeared out in case of the moving phantoms with no motion compensation. When applying motion compensation, the shape of the sphere better resembled that of the sphere in the stationary anthropomorphic phantom acquisition. The motion-compensated moving phantoms had more noise in their projection than the stationary phantom projection because the counts that are disregarded due to gating (the percentage of retained counts in the selected motion bin was 36.8% for stable motion, 33.2% for small variations, and 30.6% for large variations).

SPECT/CBCT imaging

The motion signals that were obtained during the rotation of the scanner around the anthropomorphic phantom are shown in figure 8 for the studied three motion patterns.

The SPECT reconstructions of the anthropomorphic phantoms (whole liver treatment configuration) when made with and without motion compensation are shown together with the reconstruction of the stationary anthropomorphic phantom in figure 9. The reconstructions obtained without motion compensation resulted in a blurry image. The reconstructions obtained with motion compensation were substantially sharper than the reconstructions obtained without motion compensation. The percentage of retained counts when applying motion compensation was 32.7% for the reconstructions with stable motion, 31.4% for those with small variations, and 27.8% for those with large variations.

For the quantitative evaluation, the mean difference in the activity recoveries of the four spherical inserts between the stationary phantom reconstruction and the reconstruction of interest (translating with one of three motion patterns, either uncompensated or compensated for motion) was calculated. These differences are given

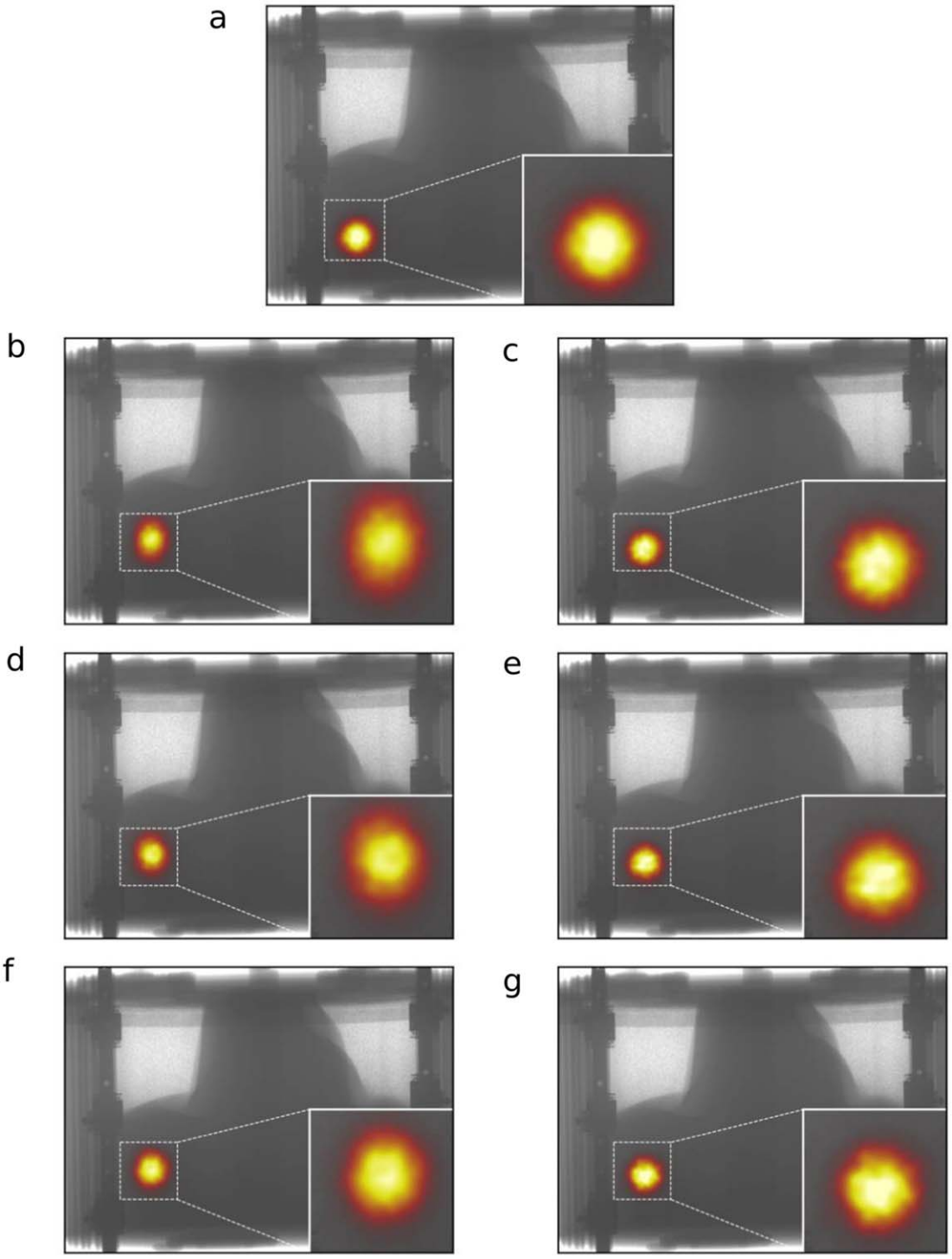

Figure 7. The nuclear projections obtained with planar imaging of the anthropomorphic phantom with the superselective treatment configuration while translating with stable motion (b), (c), small variations (d), (e), large variations (f), (g) when made without (b), (d), (f) and with (c), (e), (g) motion compensation. The projection obtained from the stationary phantom is shown in (a) as a reference.

in table 2. A lower difference indicates that the quantitative performance of the reconstruction of interest was better.

Two observations can be made. First, the reconstructions made with motion compensation consistently gave lower differences than the reconstructions made without compensation. This indicates that motion compensation accurately improved the quantitative performance of the SPECT reconstructions. And second, the improvement achieved by applying motion compensation was greatest for the anthropomorphic phantom translating with stable motion. The relative improvements became increasingly lower for the phantoms translating with small and large variations in the motion signal.

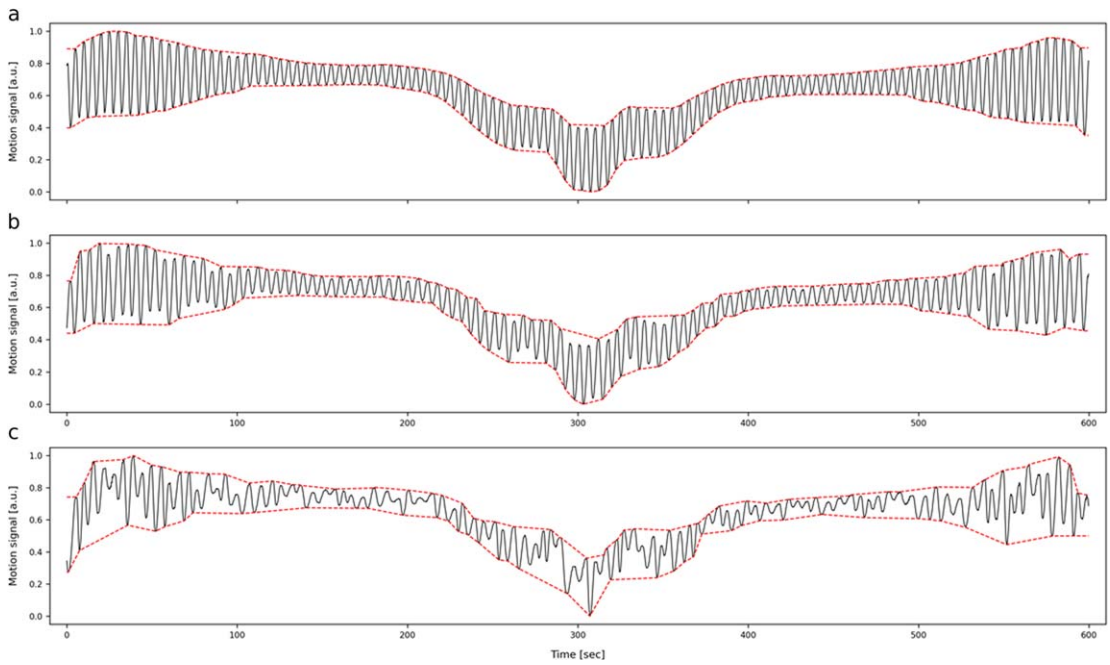

Figure 8. The motion signal that was extracted while that scanner was rotating around the anthropomorphic phantom while translating with (a) stable motion, (b) small variations, and (c) large variations. The red dashed lines denote the lower and upper bounds of the signal that are used for normalization.

Discussion

This study demonstrated the potential of performing motion compensation using a hybrid c-arm scanner that is capable of simultaneous fluoroscopic and nuclear projection acquisition using phantom experiments. The motion compensation approach has been proposed for the setting of interventional imaging, in which external devices for the motion signal extraction are undesired and data-driven approaches can be unstable due to the low count rates.

A limitation of this study was that the anthropomorphic phantom translated in only one direction and that the organ compartments did not change over the respiratory cycle. Real patient motion has translations in 3D and organ-specific translations and deformations. However, as long as these additional movements are stable over time, the motion compensation approach should provide similar results as described in this study seeing that the proposed method does not rely on any specific movement assumptions.

A further limitation of this study is that the uncertainty in the SPECT/CBCT imaging phantom analysis was only assessed by making multiple noise realization from the full list-mode data. These uncertainties hence do not include potential uncertainties in the motion signal extraction. It would be better if the entire measurement would be repeated multiple times so that these uncertainties are also included. We did not perform this methodology due to practical reasons: every measurement requires 10 min of acquisition time and needs a precise calibration between the involved systems. Nevertheless, it was demonstrated in the motion signal extraction experiments that the fluoroscopic signal extraction provides very stable results. Hence, we believe that photon noise will in the studied cases be far dominant over uncertainties in the motion signal extraction and that the approach as in this work is representative of the true setting.

Since the flat panel detector is positioned in front of the gamma camera, the source-to-collimator distance is larger for IXSI than for a conventional SPECT/CT scanner. The improvements to the quality of planar nuclear projections and the SPECT reconstructions by applying motion compensation are hence currently limited by the intrinsic spatial resolution of IXSI. When the flat panel detector thickness is reduced (e.g. by relocating the detector electronics), the intrinsic spatial resolution will improve and the relative influence of motion compensation will increase.

A limitation of the current scanner configuration is that a registration of the CBCT reconstruction with a previously-acquired attenuation map is required because of the limited FOV of the flat panel detector. Ideally, the scanner may be used a self-contained unit that does not require such a registration. This form of imaging may e.g. be realized by increasing the size of the flat panel detector or by using SPECT information to obtain an attenuation map through a form of MLAA reconstruction (Berker and Li 2016). However, for now, we believe

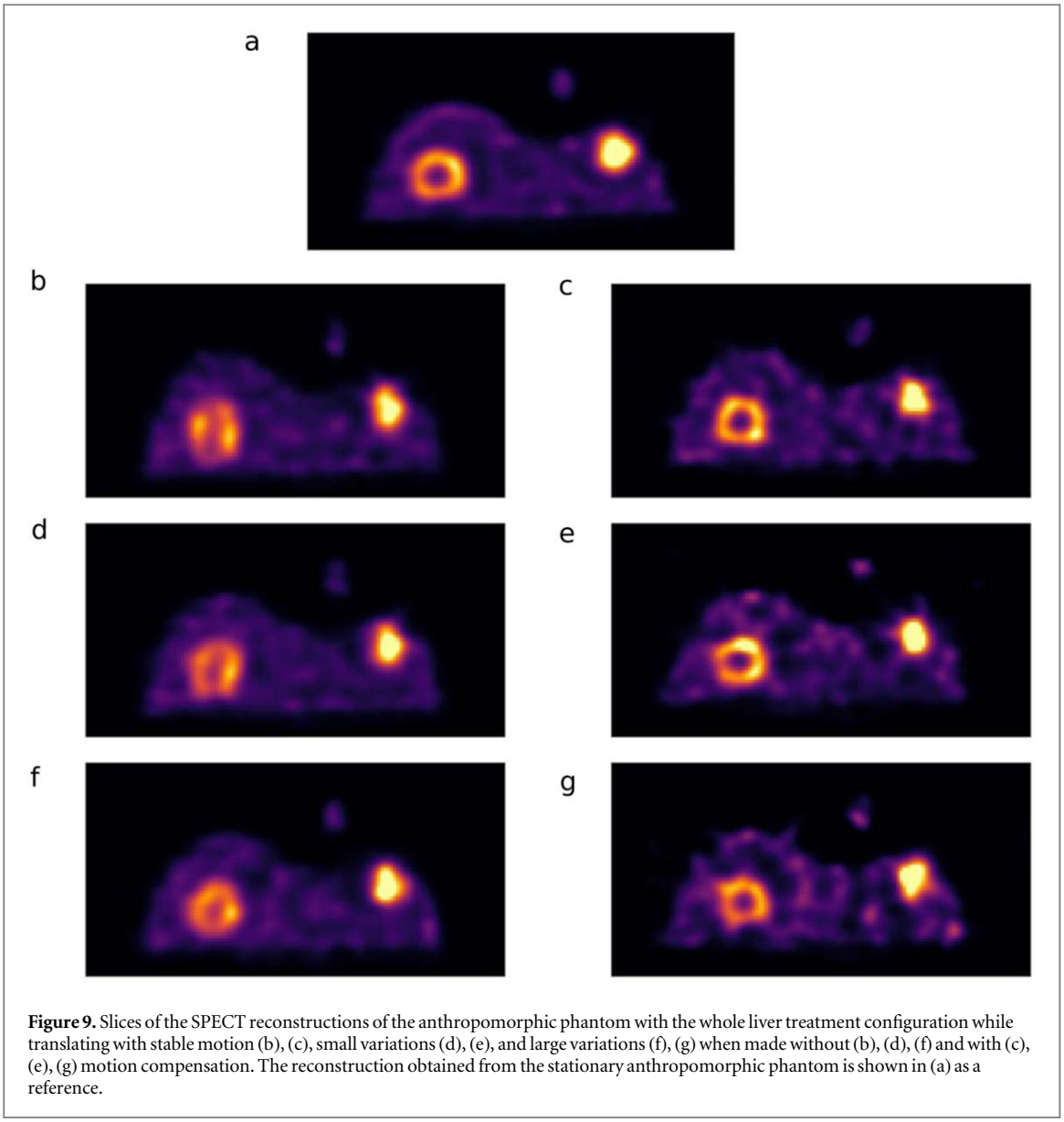

Figure 9. Slices of the SPECT reconstructions of the anthropomorphic phantom with the whole liver treatment configuration while translating with stable motion (b), (c), small variations (d), (e), and large variations (f), (g) when made without (b), (d), (f) and with (c), (e), (g) motion compensation. The reconstruction obtained from the stationary anthropomorphic phantom is shown in (a) as a reference.

Table 2. The mean difference in the activity recoveries of the four spherical inserts between the stationary phantom reconstruction and the reconstructions of interest (translating with one of three motion patterns, either uncompensated or compensated for motion). The standard deviations were determined from the 10 individually analyzed noise realizations.

	Uncompensated	Compensated
Stable	15.8% ± 0.9%	1.8% ± 1.6%
Small	11.9% ± 0.9%	2.2% ± 1.5%
Large	11.0% ± 0.9%	5.2% ± 2.5%

we can obtain fast and accurate results through the registration-based approach and we will use this methodology in the planned clinical study.

The noise in the SPECT reconstructions increases when performing motion compensation since the nuclear counts from only one motion bin are used. For the pre-treatment procedure of radioembolization (which is one of the proposed applications of IXSI), it has, however, previously been demonstrated that quantitative measures can be accurately determined even for high-noise reconstructions. van der Velden *et al* (2019a) demonstrated that activity recoveries and the lung-shunting can be accurately retrieved when using faster acquisitions (using a

one minute instead of 20 min scan duration; 20× more noise). Dietze *et al* (2020a) demonstrated that extrahepatic depositions could be accurately retrieved when using faster acquisitions (using a mean acquisition duration of five minutes instead of 20 min; 4× more noise). And Kunnen *et al* (2020) demonstrated that the use of lower activity levels can provide quantitative accurate results (imaging 100 MBq instead of 2 GBq ^{90}Y; 20× more noise). For interventional imaging, we hence believe that it is more important to obtain quantitatively correct images rather than images with low noise.

The phantom analysis performed with SPECT/CBCT imaging employed CT-based masks of the spherical inserts. When SPECT-based masks are used (e.g. by determining features in the reconstruction and growing the volume to a certain size), higher activity recoveries may be achieved and the improvement from motion compensation decreases (Bastiaannet *et al* 2017). However, the difficulty of SPECT-based masks is that sufficient contrast should be available in the reconstruction to determine the feature of interest. This contrast may not always be sufficient. Especially when moving toward voxel-based dosimetry, which is one of the goals of radioembolization, such considerations become increasingly important. For these reasons, we decided to employ a CT-based mask in this study.

Due to the cone beam geometry of the fluoroscopic projections, the position of the diaphragm changes during the rotation of the scanner around the phantom in the SPECT/CBCT imaging experiment. This effect causes a baseline-shift of the motion signal over time (see e.g. figure 8(a)). However, at the same time, there might be a baseline-shift in the motion signal itself due to irregular breathing (see e.g. figures 3(b), (c)). It is not possible to distinguish these two effects and, for this reason, the proposed motion compensation approach provides lower improvements for irregular breathing movements (as shown in table 2). It is likely that a substantial fraction of patients will have variations in their respiratory breathing amplitude. A planned clinical study will study to which extent the proposed motion compensation method will be beneficial for patients undergoing the pre-treatment procedure of hepatic radioembolization.

It might also be possible to extract a motion model from the motion-binned CBCT reconstructions so that it can be incorporated in the SPECT reconstruction. This approach has the advantage that no counts are disregarded and hence that the noise in the reconstruction is kept low. The approach was successfully demonstrated with digital simulations (Dietze *et al* 2019a) but proved to be challenging due to the relatively low quality of the CBCT reconstruction when imaging at a low dose. Furthermore, the approach required several assumptions on the movement of the organs in the body, which may not necessarily hold in patients. Thus, although the performance of the motion-model approach will also be investigated when IXSI is employed in patient studies, the gating approach as in this study will be the primary objective for now.

For the case of interventional imaging as is proposed in this work, many fluoroscopic images are already acquired for either planar procedural guidance or for the retrieval of the attenuation map. The proposed motion compensation method simultaneously uses these images for the determination of the motion signal. In this setting, (almost) no additional fluoroscopic dose is hence administered to the patient when applying motion compensation. For other cases (e.g. conventional diagnostic SPECT), the proposed motion compensation method will administrate an additional fluoroscopic dose to the patient. For reference of the involved dose levels, imaging at 60 kVp for 15 min (e.g. planar imaging for 5 min and SPECT/CBCT for 10 min) resulted in a DAP of 0.8 mGy m^2. The additional fluoroscopic dose from the proposed motion compensation method may be decreased by lowering the x-ray tube strength to 50 kVp (since this setting gave approximately the same performance as 60 kVp).

Conclusion

Phantom experiments demonstrated that a hybrid c-arm scanner, capable of simultaneous nuclear and fluoroscopic projection acquisition, can perform compensation for respiratory motion in interventional imaging. Motion compensation improved the interpretation of the planar nuclear projections and increased the quantitative accuracy of the SPECT reconstructions. The improvement achieved by applying motion compensation was greatest for the stable motion pattern and became increasingly lower for the motion patterns with small and large variations.

Disclosure

This project has received funding from the European Research Council (ERC) under the European Union's Horizon 2020 research and innovation program grant agreement No. 646734. Philips Healthcare supported this research by providing an adapted flat panel detector and providing software for the CBCT reconstruction. The authors had full control over the data and the information submitted for publication.

ORCID iDs

Martijn M A Dietze https://orcid.org/0000-0003-1159-3510

References

Bastiaannet R, Viergever M A and de Jong H W A M 2017 Impact of respiratory motion and acquisition settings on SPECT liver dosimetry for radioembolization *Med. Phys.* **44** 5270–9

Berker Y and Li Y 2016 Attenuation correction in emission tomography using the emission data—a review *Med. Phys.* **43** 807–32

Braat A J A T, Smits M L J, Braat M N G J A, van den Hoven A F, Prince J F, de Jong H W A M, van den Bosch M A A J and Lam M G E H 2015 ^{90}Y hepatic radioembolization: an update on current practice and recent developments *J. Nucl. Med.* **56** 1079–87

Cho K, Kumiata S, Okada S and Kumazaki T 1999 Development of respiratory gated myocardial SPECT system *J. Nucl. Cardiol.* **6** 20–8

Dietze M M A, Bastiaannet R, Kunnen B, van der Velden S, Lam M G E H, Viergever M A and de Jong H W A M 2019a Respiratory motion compensation in interventional liver SPECT using simultaneous fluoroscopic and nuclear imaging *Med. Phys.* **46** 3496–507

Dietze M M A, Kunnen B, Beijst C and de Jong H W A M 2020a Adaptive scan duration in SPECT: evaluation for radioembolization *Med. Phys.* **47** 2128–38

Dietze M M A, Kunnen B, Stella M and de Jong H W A M 2020b Monte Carlo-based scatter correction for the SMARTZOOM collimator *EJNMMI Phys.* **7** 49

Dietze M M A, Kunnen B, van der Velden S, Steenbergen J H L, Koppert W J C, Viergever M A and de Jong H W A M 2019b Performance of a dual-layer scanner for hybrid SPECT/CBCT *Phys. Med. Biol.* **64** 105020

Dietze M M A, van der Velden S, Lam M G E H, Viergever M A and de Jong H W A M 2018 Fast quantitative reconstruction with focusing collimators for liver SPECT *EJNMMI Phys.* **5** 28

Klein S, Staring M, Murphy K, Viergever M A and Pluim J P W 2010 Elastix: a toolbox for intensity-based medical image registration *IEEE Trans. Med. Imaging* **29** 196–205

Koppert W J C, Dietze M M A, van der Velden S, Steenbergen J H L and de Jong H W A M 2019 A comparative study of NaI(Tl), CeBr3, and CZT for use in a real-time simultaneous nuclear and fluoroscopic dual-layer detector *Phys. Med. Biol.* **64** 135012

Koppert W J C, van der Velden S, Steenbergen J H L and de Jong H W A M 2018 Impact of intense x-ray pulses on a NaI(Tl)-based gamma camera *Phys. Med. Biol.* **63** 065006

Kunnen B, Dietze M M A, Braat A J A T, Lam M G E H, Viergever M A and de Jong H W A M 2020 Feasibility of imaging 90Y microspheres at diagnostic activity levels for hepatic radioembolization treatment planning *Med. Phys.* **47** 1105–14

McClelland J R, Hawkes D J, Schaeffter T and King A P 2013 Respiratory motion models: a review *Med. Image Anal.* **17** 19–42

Mukherjee J M, Hutton B F, Johnson K L, Pretorius P H and King M A 2013 An evaluation of data-driven motion estimation in comparison to the usage of external-surrogates in cardiac SPECT imaging *Phys. Med. Biol.* **58** 7625–46

Murase K, Ishine M, Kataoka M, Itoh H, Mogami H, Iio A and Hamamoto K 1987 Simulation and experimental study of respiratory motion effect on image quality of single photon emission computed tomography (SPECT) *Eur. J. Nucl. Med.* **13** 244–9

Nehmeh S A and Erdi Y E 2008 Respiratory motion in positron emission tomography/computed tomography: a review *Semin. Nucl. Med.* **38** 167–76

Pretorius P H, Johnson K L, Dahlberg S T and King M A 2020 Investigation of the physical effects of respiratory motion compensation in a large population of patients undergoing Tc-99m cardiac perfusion SPECT/CT stress imaging *J. Nucl. Cardiol.* **27** 80–95

Sanders J C, Ritt P, Kuwert T, Vija A H and Maier A K 2016 Fully automated data-Driven respiratory signal extraction from SPECT images using laplacian eigenmaps *IEEE Trans. Med. Imaging* **35** 2425–35

Turner D A *et al* 1978 Motion corrected hepatic scintigraphy: an objective clinical evaluation *J. Nucl. Med.* **19** 142–8

van der Velden S, Dietze M M A, Viergever M A and de Jong H W A M 2019a Fast technetium-99m liver SPECT for evaluation of the pretreatment procedure for radioembolization dosimetry *Med. Phys.* **46** 345–55

van der Velden S, Kunnen B, Koppert W J C, Steenbergen J H L, Dietze M M A, Beijst C, Viergever M A, Lam M G E H and de Jong H W A M 2019b A dual-layer detector for simultaneous fluoroscopic and nuclear imaging *Radiology* **290** 833–8

Vidal-Sicart S, Paredes P, Zanón G, Pahisa J, Martinez-Román S, Caparrós X, Vilalta A, Rull R and Pons F 2010 Added value of intraoperative real-time imaging in searches for difficult-to-locate sentinel nodes *J. Nucl. Med.* **51** 1219–25

Zhang D, Pretorius P H, Ghaly M, Zhang Q, King M A and Mok G S P 2020 Evaluation of different respiratory gating schemes for cardiac SPECT *J. Nucl. Cardiol.* **27** 634–47